

NEW ESTIMATORS OF BLACK HOLE MASS IN ACTIVE GALACTIC NUCLEI WITH HYDROGEN PASCHEN LINES

Dohyeong Kim¹, Myungshin Im¹ AND Minjin Kim²

Draft version November 2, 2018

ABSTRACT

More than 50% of Active Galactic Nuclei (AGNs) are suspected to be red and affected by dust-obscuration. Meanwhile, popular spectral diagnostics of AGNs are based on optical or ultraviolet light, making the dust obscuration as a primary concern for understanding the general nature of AGNs and supermassive black holes residing in them. To provide with a method of investigating properties of the dusty AGNs, we derive new black hole (BH) mass estimators based on velocity widths and luminosities of Near Infrared (NIR) hydrogen emission lines such as P α and P β , and also investigate the line ratios of these Hydrogen lines. To derive the BH mass (M_{BH}) estimators, we used a sample of 37 unobscured Type-1 AGNs with a M_{BH} range of $10^{6.8}$ – $10^{9.4} M_{\odot}$, where M_{BH} come from either reverberation mapping method or single-epoch measurement method using Balmer lines. Our work shows that M_{BH} can be estimated from the Paschen line luminosities and the velocity widths to the accuracy of 0.18 - 0.24 dex (rms scatter). We also show that the mean line ratios of the Paschen lines and the Balmer lines are $\frac{H\alpha}{P\alpha} \simeq 9.00$, $\frac{H\beta}{P\alpha} \simeq 2.70$, which are consistent with a Case B recombination under a typical AGN broad line region environment. These ratios can be used as reference points when estimating the amount of dust extinction over the broad line region (BLR) for red AGNs. We expect the future application of the new BH mass estimators on red, dusty AGNs to provide a fresh view of obscured AGNs.

Subject headings: black hole, AGN, dusty AGN, NIR, Paschen line

1. INTRODUCTION

Supermassive black holes (SMBHs), found at centers of massive spheroids and active galaxies, are considered to play an important role in the formation and the evolution of galaxies. It is suggested that SMBHs regulate the star formation activities of galaxies through their enormous energy output during active phase, providing a feedback mechanism to reconcile the observed trend of downsizing of the galaxy evolution with hierarchical galaxy formation models (Juneau et al. 2005; Bundy et al. 2006; Schawinski et al. 2006). However, the coevolution of SMBHs and their host galaxies stand as an unsolved astrophysical problem, as such a process needs to eventually lead to a rather unexpected tight correlation between host galaxy properties and SMBH mass today (Ferrarese & Merritt 2000; Gebhardt et al. 2000; Tremaine et al. 2002).

One of the great challenges toward the understanding of the evolutionary sequence of AGNs and the co-evolution of SMBHs and their host galaxies comes from the so-called red or dusty AGNs which are believed to occupy more than 50% of the AGN population (Comastri et al. 2001; Tozzi et al. 2006; Polletta et al. 2008). Red, dusty AGNs are expected, if the initial phase of AGN activity starts in a dust-enshrouded environment such as within massive starburst regions of luminous infrared galaxies. In such a scenario, AGNs become more visible after sweeping away cold gas and dust that are

necessary to sustain the massive star formation in their host galaxies (Hopkins & Hernquist 2006). On the other hand, dust obscuration can arise in a different way in the unified model of AGN when accretion disks and broad line regions (BLRs) around SMBHs are viewed through dust torus. In any case, red, dusty AGNs can shed light on the properties and the evolution of the AGN population in general.

The phenomenological definition of “red, dusty AGNs” is rather broad. It can include AGNs selected in a variety of ways such as those selected by very red colors in optical through NIR and the radio detection (e.g., $R - K > 5$ mag and $J - K > 1.3$ mag of the sample in Urrutia et al. 2009; also see Cutri et al. 2001), red MIR colors (Lacy et al. 2004; Lee et al. 2008), and hard X-ray detections (e.g., Polletta et al. 2007). These different kinds of AGNs have a common characteristic where their SEDs are red, due to the obscuration of their light by the foreground gas and dust. Hence, they are considered to be the intermediate population between the dust-enshrouded star forming galaxies and the unobscured AGNs. The dust-obscuration does not necessarily exclude Type-1 AGNs (AGNs with broad emission lines; e.g., Alonso-Herrero et al. 2006), as red, dusty AGNs with broad emission lines are found quite often. Of 23 X-ray QSOs with IR power-law SED and spectroscopic redshift identification, 14 are classified as broad-line AGNs (Szokoly et al. 2004; Alonso-Herrero et al. 2006). More than 50% of the red AGNs with the radio and red optical/NIR color selection are found to be type-1 AGN which can have the reddening parameter of 2 or more (Urrutia et al. 2009; Glikman et al. 2007). The existence of broad line AGNs among red, dusty AGNs opens a possibility of studying the properties of the dust-obscured quasars in more detail using

¹ Center for the Exploration of the Origin of the Universe (CEOU), Astronomy Program, Department of Physics and Astronomy, Seoul National University, Shillim-Dong, Kwanak-Gu, Seoul 151-742, South Korea

² National Radio Astronomy Observatory, 520 Edgemont Road, Charlottesville, VA 22903, USA

traditional type-1 AGN diagnostics.

However, even the measurement of the most basic AGN parameters such as M_{BH} and the Eddington ratio (the accretion rate) is a difficult task for the red, dusty AGNs. In general, M_{BH} are derived from the optical or the ultraviolet (UV) part of AGN spectra for which spectral diagnostics are well established. In the case of dusty AGNs, the dust obscures or significantly reduces the UV or the optical light coming from the region around SMBHs, making the popular AGN optical/UV spectroscopic diagnostics useless. For example, popular M_{BH} estimators are based upon a virial relation between two parameters - the velocity width of the broad, $\text{H}\alpha$ or $\text{H}\beta$ lines, and the size of BLR estimated from the continuum luminosity at 5100 \AA (Kaspi et al. 2000) or the luminosities of $\text{H}\alpha$ or $\text{H}\beta$ (Greene & Ho 2005). If the light from a red, dusty AGN is extinguished by a color excess of $E(B - V) = 2 \text{ mag}$ (Glikman et al. 2007; Urrutia et al. 2009), its $\text{H}\alpha$ and $\text{H}\beta$ line fluxes would be suppressed by a factor of 100 and 1000 respectively. One can try to estimate the amount of the dust extinction from a continuum fitting of the optical-UV spectrum or through the Balmer decrement, but such estimates are often inconsistent with each other and accompanied with uncertainties of order of $\delta E(B - V) \sim 0.5 \text{ mag}$ or more which are related to the dispersion in the intrinsic properties of AGNs. The dust obscuration can arise from the Galactic extinction for AGNs at low galactic latitude (e.g., Im et al. 2007; Lee et al. 2008).

The problem can be substantially alleviated if we can use NIR lines instead of optical or UV lines, since NIR Hydrogen lines such as the $\text{P}\alpha$ and $\text{P}\beta$ are much less affected by the dust extinction than the UV/optical light. For the red, dusty AGN with the color excess of $E(B - V) = 2 \text{ mag}$, the line fluxes of $\text{P}\alpha$ and $\text{P}\beta$ are suppressed by a factor of only 2.3 and 4.7 respectively. This is a significant improvement over the optical lines. Since $M_{\text{BH}} \propto L^{0.5}$, where L is a luminosity of the continuum or an emission line, the suppression in the Paschen line luminosities introduces uncertainties in M_{BH} estimates only at the level of a factor of 2 or less, even without correcting for the dust extinction with the Paschen decrement.

In this paper, we will derive the M_{BH} estimators based on the NIR Hydrogen lines of Type-1 AGNs and investigate the line ratios of the Paschen lines, keeping in mind future applications of such relations to studies of dusty, red AGNs with broad emission lines.

2. DATA

2.1. The Sample

In order to construct mass estimators based on the NIR Hydrogen lines, we used two samples of low redshift Type-1 AGNs with NIR spectra at $0.8\text{--}4.1 \mu\text{m}$. One is from Landt et al. (2008; hereafter L08) who studied 23 well-known Type-1 AGNs in the local universe. Among these, we use 16 and 21 AGNs that have line flux and width measurements in $\text{P}\alpha$ or $\text{P}\beta$ lines, respectively. Note that we excluded four objects, Mrk 590, NGC 5548, Ark 564, and NGC 7469 in all or some of our analysis even though $\text{P}\alpha$ and $\text{P}\beta$ line flux and FWHM measurements were available. For Ark 564 and NGC 7469, the FWHM values of $\text{P}\alpha$ and $\text{P}\beta$ lines listed in

L08 are too discrepant from each other differing by more than a factor of 1.5. This suggests that one of the two measurements is erroneous. Therefore, these two objects are excluded from all of the analysis performed below. For Mrk 590 and NGC 5548, the $\text{H}\alpha$ and the $\text{H}\beta$ widths listed in L08 differ by more than a factor of 1.5, but the Paschen line widths are consistent with each other. These two objects are excluded in the analysis of the correlation between the Paschen and the Balmer lines, but their reverberation-mapping derived M_{BH} are retained for the derivation of the black hole estimators (of the method 2 and the method 3 in Section 3.2).

Another sample comes from Glikman et al. (2006; hereafter G06). The G06 sample is made of 26 Type-1 AGNs that were selected from a cross-match between the SDSS-DR1 quasar catalog (Schneider et al. 2003) and the 2 micron All Sky Survey (2MASS; Skrutskie et al. 2006), with the criteria of $K < 14.5 \text{ mag}$, redshift $z < 0.5$ and the absolute magnitude in i -band, $M_i < -23 \text{ mag}$. Here, the absolute magnitude limit is imposed to minimize contamination of the quasar light due to the host galaxy. The G06 sample provides 11 AGNs with $\text{P}\alpha$ lines and 14 AGNs with $\text{P}\beta$ lines showing up in their NIR spectra.

In all, we use 27 and 35 Type-1 AGNs for the $\text{P}\alpha$ and the $\text{P}\beta$ line analysis, respectively. Table 1 summarizes properties of these AGNs.

2.2. Black Hole Mass and Analysis of Optical Spectra

For M_{BH} of our sample AGNs, we use the following values.

First, we use M_{BH} derived with the reverberation mapping method from literatures if available. This applies to 10 AGNs with $\text{P}\alpha$ and 11 AGNs $\text{P}\beta$ data in L08 for which M_{BH} are taken from Vestergaard & Peterson (2006).

Second, if M_{BH} from the reverberation mapping method are not available, we derived M_{BH} from the optical spectral information using single epoch M_{BH} estimators. For the L08 sample without the reverberation mapping derived M_{BH} , we used the $\text{H}\beta$ luminosity and FWHM listed in the Table 5 of L08 to derive their M_{BH} . For this, we adopted a M_{BH} estimator in Greene & Ho (2005), after adjusting their relation to have the virial factor of 5.5 (Onken et al. 2004; Woo et al. 2010) by multiplying their relation by a factor of 1.8. We also made a small correction to the L08 FWHM and luminosity values, since the way how Greene & Ho (2005) derived FWHMs and luminosities is different from what L08 did - Greene & Ho (2005) adopted a multiple Gaussian component fitting to the broad line while L08 adopted a single component fitting of the broad line after removing narrow line components. We find that the correction factor to be $\text{FWHM}_{\text{multi}}/\text{FWHM}_{\text{single}}=0.9$ and $L_{\text{multi}}/L_{\text{single}}=1.08$ on average through fitting of the SDSS spectra of the G06 sample with the two methods (See below).

For the G06 sample, none of the objects have M_{BH} derived from the reverberation mapping method. Some of the G06 sample have their $\text{H}\beta$ line luminosities and FWHMs listed in Shen et al. (2008), but after checking FWHM values in Shen et al. (2008) and the optical spectra, we find cases where FWHMs appear to be overestimated. Therefore, we used our own spectral fitting routine (Kim et al. 2006) to obtain the $\text{H}\beta$ FWHMs and

the $H\beta$ luminosities from the SDSS spectra. The fitting model includes components for a power law continuum, the host galaxy light, broad Fe II multiplet emissions, a Balmer continuum, and multiple Gaussian profiles for broad and narrow emission lines. The FWHM and the line luminosities are derived from the best-fit model profiles of the broad line component which can be consisted of a sum of multiple Gaussian components.

From the derived luminosity and FWHM values, we estimated M_{BH} by using an updated version of the $H\beta$ -based virial mass estimator (Greene & Ho 2005). We updated Equation (7) in Greene & Ho (2005), by adopting a newer $R_{\text{BLR}}-L_{5100}$ relation, i.e., Equation (2) of (Bentz et al. 2009). The updated relation is given below.

$$\frac{M}{M_{\odot}} = 10^{6.88 \pm 0.57} \left(\frac{L_{H\beta}}{10^{42} \text{ erg s}^{-1}} \right)^{0.46 \pm 0.05} \left(\frac{\text{FWHM}_{H\beta}}{10^3 \text{ km s}^{-1}} \right)^2. \quad (1)$$

Again, a proper adjustment was made for the virial factor in order to make the relation consistent with the virial factor in Vestergaard & Peterson (2006). The derived BH masses are listed in Table 1.

2.3. Analysis of NIR Spectra and Line Information

The G06 data were taken mostly with the SpeX instrument on the IRTF with the spectral resolution of $\frac{\Delta\lambda}{\lambda} \simeq 1200$ at 0.8 - 2.5 μm , and $\frac{\Delta\lambda}{\lambda} \simeq 1500$ at 1.9 - 4.1 μm . G06 provide with the flux-calibrated, reduced NIR spectra, and we used the following procedure to measure the Paschen line fluxes and FWHMs of the G06 sample.

The G06 spectra were converted to the rest-frame, and then the continuum around the Paschen lines were determined by fitting a linear function to the continuum at regions near the Paschen lines. We varied the wavelength centers and widths of the continuum fitting regions, but typical values are chosen to be ~ 2 FWHM of the broad component of $H\beta$ line away from the Paschen line center and the width of 0.02 μm for the continuum fitting region centers and widths respectively. For the $P\alpha$ line, this corresponds to the wavelength regions centered somewhere at 1.82 to 1.84 μm and 1.90 to 1.92 μm with the width of 0.02 μm , while for the $P\beta$ line the wavelength centers are somewhere at 1.23 to 1.25 μm and 1.31 to 1.33 μm . When the continuum shows data points affected by imperfect sky subtraction, we adjusted the continuum fitting regions. Also, the width of the continuum fitting regions are varied from 0.01 to 0.03 μm , and the center wavelengths are shifted by 0.01-0.02 μm to provide robust measurements. Although NIR spectra of Type-1 AGNs are known to be dominated by a black body radiation from warm dust, we find that the linear fitting of the continuum over the limited wavelength range provides a reasonable approximation of the continuum around the Paschen lines (see Figure 2; also see L08).

After the continuum subtraction, we used a single Gaussian function to fit an emission line. The fitted parameters are multiplied by correction factors to correct for systematic errors in the single component fitting (see next paragraph). During the fitting, we set free the central wavelength of each Gaussian component. Therefore, the free parameters of the fit are FWHM, flux, and the central wavelength for Gaussian component. The fit was

performed with the MPFITEXPR procedure of the IDL. Figures 2 and 3 show the line-fitting results. The fits provide a formal error of 12% in flux and 9% in FWHM. We also estimated the error arising from uncertainties related to how the continuum is determined. This was done by varying the regions for the continuum fitting as described earlier. We find that the average uncertainty arising from the continuum determination is 4% (flux), 3% (FWHM), although we find cases where the FWHM values change by as much as 25%. Such cases occur when there is an extended feature at the wing of the emission line which may or may not be a true feature. The total errors in flux and FWHM measurement are taken as a square root of the quadratic sum of the formal fitting error and the error from the continuum determination, which are found to be typically 12% and 9%.

Fitting a multiple component line with a single Gaussian function can produce systematic errors in the fitted parameters, and we tried to correct for such a bias by applying correction factors that are derived from Balmer lines. This is done by comparing the broad line widths and the line fluxes from multiple component fits of Balmer lines versus the fitted parameters from a single component fit of the same Balmer lines. By doing so, we correct potential systematic arising from not removing narrow line components in the fitting process too. The correction factors are computed for each object and they range over 0.74 - 1.01 with the mean of 0.91 for the FWHM ratios ($\text{FWHM}_{\text{multi}}/\text{FWHM}_{\text{single}}$) and 0.98 - 1.17 for the line flux ratio with the mean of 1.06 ($L_{\text{multi}}/L_{\text{single}}$). This procedure makes an assumption that the line profile shapes of the Paschen lines follow those of the Balmer lines. To confirm this assumption, we compared the $P\beta$ line profiles with the model-fitted line profiles of $H\alpha$. Only the $P\beta$ lines with the S/N > 25 are shown in Figure 4. The $P\beta$ lines are plotted as histograms with error bars, while the $H\alpha$ lines are indicated with thick solid lines. The thin dotted lines and the thick dashed lines represent the broad and the narrow components of the $H\alpha$ lines. The $P\beta$ profiles are normalized to have the maximum value of 1 while the $H\alpha$ are normalized to have the same total flux as the normalized $P\beta$ profiles. Figure 4 demonstrates that the $P\beta$ profile shapes are consistent with those of the $H\alpha$ profiles, except for the width and the overall normalization, supporting our assumption that the Paschen line profiles are similar to those of the Balmer lines. We also tried fitting the Paschen line profiles with double Gaussian profiles for objects that seem to have narrow line components (SDSSJ010226.3-003904.6, SDSSJ015530.0-085704.0, SDSSJ015950.2+002340.8, SDSSJ031209.2-081013.8, SDSSJ015910.0+010514.5, SDSSJ235156.1-010913.3, SDSSJ000943.1-090839.2 and SDSSJ011110.0-101631.8). For $H\beta$, we find that the double Gaussian fitting returns FWHM values greater than those from the single Gaussian fitting by a factor of 1.08 in average. However, the double Gaussian fitting (one for narrow line, and another for broad line) tends to return FWHM values greater than the results from the multiple component fitting. Thus, another correction factor is needed to convert the double Gaussian fitting result to the multiple Gaussian fitting result, and the result from this double Gaussian fitting test should be taken seriously. We are presenting a result

from this test in order to see if we find the same kind of the dependency of fitted parameters on the fitting method which we find in the Balmer lines as a way to support our assumption that the Paschen line profiles are similar to the Balmer line profiles.

In most case, the fitted values from the double component fit agree with those from the single component fit (without the additional correction factor), where the FWHM and flux values from the double component fittings are in average 7% larger and 2% smaller than the single component fitting results respectively. This agrees well with the trend we find from our analysis of the Balmer lines using single, double, and multiple component Gaussian fittings (see above). One exception is SDSSJ015950.2+002340.8 whose FWHM changed by about 50%. Distinguishing the narrow and the broad components is difficult for this object, therefore the mean value between the parameters from the two different methods was adopted as the best-fit value, with the half of the difference as its error. We note that the double component fit improved the reduced χ^2 values significantly (> 0.3) for only three objects, where the improvement came from fitting of broad extended wings which did not affect the derived fitting parameter values rather than through the change of the FWHM values (except for SDSSJ015950.2+002340.8).

Finally, the measured FWHMs were corrected for the instrumental resolution and the fitting methodology (multiple component fit versus single component fit), and the fluxes were converted to the luminosity assuming a standard Λ CDM cosmology of $H_0=70$ km sec $^{-1}$ Mpc $^{-1}$, $\Omega_m=0.3$ and $\Omega_\Lambda=0.7$ (e.g., Im et al. 1997). The measured line luminosities, fluxes, and FWHMs are presented in Table 1.

L08 present the results of their line analysis, based on the NIR spectra that were taken with the Spex spectrograph (Rayner et al. 2003) on the Infrared Telescope Facility (IRTF) at an average spectral resolution of 400 km s $^{-1}$. For the L08 sample, we use the line fluxes and FWHMs derived by them and presented in their Table 1, after correcting FWHM values for the instrumental resolution. We also applied the correction factor of $\text{FWHM}_{\text{multi}}/\text{FWHM}_{\text{singlebroad}}=0.9$ and $L_{\text{multi}}/L_{\text{singlebroad}}=1.08$ which corrects for the difference in the line-fitting methods (L08 versus Greene & Ho 2005) to derive the line parameters which are similar to the correction factors we derived for the fitting process of the G06 spectra. As for the accuracy of the L08 measurements, L08 quote a typical error of 10% or less. Therefore, we adopt a conservative value of 10% for the measurement error of the fluxes and the FWHMs presented in L08.

We note that contamination from the host galaxy light to these measurements is negligible. The contamination of the line flux due to the host galaxy is possible, but the G06 data were taken with a narrow slit to minimize the host galaxy light to less than 8%. We expect that the same statement holds true for the L08 sample whose data were taken with a narrow slit for AGNs at $z < 0.1$ which are located much closer to us than the G06 sample.

3. RESULTS

3.1. Empirical Relation between Balmer and Paschen Lines

Before constructing mass estimators based on the Paschen lines, we show here that how well the properties of the Paschen lines correlate with the Balmer lines. A tight correlation between the two lines would imply that the Paschen lines originate from the broad line regions similar to the Balmer lines, thus serving as a strong justification for the use of the Paschen lines as a mass estimator. Good correlations between the FWHM values of the broad Balmer lines and the broad Paschen lines were shown in L08. Here, we extend the analysis to the line flux ratios, and add quasars from the G06 sample to the L08 sample to strengthen the goodness of the FWHM correlation. Furthermore, we also derive equations that relate the properties of the Balmer and the Paschen lines. Figure 5 shows the correlation between FWHM values of the Balmer and the Paschen broad lines, while Figure 6 shows a correlation of line luminosities of the broad lines. To derive the correlations between the two quantities, we performed a linear bisector fit using the equations below.

$$\log\left(\frac{\text{FWHM}_Y}{1000 \text{ km s}^{-1}}\right) = A + B \log\left(\frac{\text{FWHM}_X}{1000 \text{ km s}^{-1}}\right) \quad (2)$$

$$\log\left(\frac{L_Y}{10^{42} \text{ erg s}^{-1}}\right) = C + D \log\left(\frac{L_X}{10^{42} \text{ erg s}^{-1}}\right) \quad (3)$$

Here, X and Y are line identifiers, and A and B are the correlation coefficients in the fit for FWHM, and C and D are the coefficients for the line luminosity ratio fit. The results of the fitting are summarized in Table 2. The table also lists the rms scatter of the data points with respect to the best-fit lines.

These results show that the Paschen line luminosities and FWHMs correlate well with those of the Balmer lines. The rms scatters in the line luminosity correlation are ~ 0.12 - 0.14 dex against $H\alpha$, and ~ 0.16 - 0.19 dex against $H\beta$. For the FWHM values, the rms scatters are 0.045 - 0.06 dex against $H\alpha$, and 0.05 - 0.06 dex against $H\beta$. The slightly larger scatters and a notable offset in FWHM values of $H\beta$ against Paschen lines suggest the complexities in AGN spectra around $H\beta$ line noted in L08, an excess, broad component in the red part of the $H\beta$ line caused by an unclear origin (e.g., Meyers & Peterson 1985; Véron et al. 2002). We also point out that the line widths of Balmer lines are systematically larger than those of the Paschen lines, and that the trend is stronger as the wavelength decreases. This suggests that the Paschen broad lines and the Balmer broad lines originate from a similar BLR, but with Balmer lines originating from the inner region of the BLR than Paschen lines.

Similarly, we also examine correlations between ($L_{5100\text{\AA}}$) and $L_{P\alpha,\beta}$. R_{BLR} values are derived from $L(5100)$ using Equation (4) of (Greene & Ho 2005). Figure 7 shows the correlation between R_{BLR} and Paschen line luminosities, and Equations (4) and (5) are the best-fit results.

$$R_{\text{BLR}} = (50.5 \pm 1.0) \left(\frac{L_{P\alpha}}{10^{42} \text{ erg s}^{-1}} \right)^{(0.40 \pm 0.01)} \text{ lt - days}, \quad (4)$$

$$R_{\text{BLR}} = (50.6 \pm 1.0) \left(\frac{L_{P\beta}}{10^{42} \text{ erg s}^{-1}} \right)^{(0.48 \pm 0.01)} \text{ lt - days}. \quad (5)$$

Figure 7 and the above result indicate that the luminosity of the Paschen lines is closely connected to the radius of BLR.

These tight correlations support the idea that the Paschen line emissions originate from the BLR region similar to the area where the broad lines of the Balmer lines arise. Thus, it should be possible to derive M_{BH} from $P\alpha$ and $P\beta$ just like M_{BH} can be estimated from $H\beta$ and $H\alpha$. Now, we move on to the derivation of M_{BH} estimators based on Paschen lines.

3.2. Mass Estimators

In this section, we derive new M_{BH} estimators based on $P\alpha$ and $P\beta$ lines over the mass range of $10^{6.4} \sim 10^{9.5} M_{\odot}$. These M_{BH} estimators are analogous to the M_{BH} estimators based on $H\alpha$ and $H\beta$ lines (Greene & Ho 2005), with $L_{P\alpha}$ and $L_{P\beta}$ serving as a measure of the BLR size, and FWHMs of the Paschen lines as the velocity term in the virial mass estimator. Mathematically, we need find three unknown parameters, a , b , and c in the following equation.

$$\log(M) = a + b \log(L) + c \log(\text{FWHM}) \quad (6)$$

The expected values are $c = 2$ from the virial theorem, and $b = 0.5$ if $L \sim R_{\text{BLR}}^2$ (Dibai 1977). Since there are several ways to derive M_{BH} estimators and the results may not be identical, we derive M_{BH} estimators in three different ways as described below.

First, we derive M_{BH} estimators by simply replacing the line luminosities and FWHMs of the Hydrogen Balmer line mass estimators (A1) of (Greene & Ho 2007) with those of the Paschen lines using the relation presented in Section 3.1. We used the $H\alpha$ -based M_{BH} estimator since the comparison of $H\alpha$ and the Paschen line properties show smaller scatter values than $H\beta$. We replaced the $H\alpha$ luminosity and FWHM in the base estimator with those of $P\alpha$ or $P\beta$ lines. A factor of 1.8 is multiplied to the $H\alpha$ -based M_{BH} estimator of Greene & Ho (2005) so that the new relation is normalized to the virial factor of $f = 5.5$. The M_{BH} values for the left-hand side of Equation (6) are those listed in Table 1. The Paschen line based M_{BH} estimators derived this way are given below.

$$\frac{M}{M_{\odot}} = 10^{7.29 \pm 0.10} \left(\frac{L_{P\alpha}}{10^{42} \text{ erg s}^{-1}} \right)^{0.43 \pm 0.03} \left(\frac{\text{FWHM}_{P\alpha}}{10^3 \text{ km s}^{-1}} \right)^{1.92 \pm 0.18} \quad (7)$$

$$\frac{M}{M_{\odot}} = 10^{7.33 \pm 0.10} \left(\frac{L_{P\beta}}{10^{42} \text{ erg s}^{-1}} \right)^{0.45 \pm 0.03} \left(\frac{\text{FWHM}_{P\beta}}{10^3 \text{ km s}^{-1}} \right)^{1.69 \pm 0.16} \quad (8)$$

Figure 8 shows M_{BH} from this estimator versus the input M_{BH} values. The estimators provide a reasonable

fit with rms scatter of 0.22, 0.23 dex for both M_{BH} ($P\alpha$) and M_{BH} ($P\beta$).

The second and the third methods utilize a direct fit of the M_{BH} values. In the second method, we fix the exponent of the velocity term c to 2 as expected in the virial relation, while setting the overall normalization, a , and the exponent of the luminosity term, b , as free parameters. For this, we performed a linear regression fit in logarithmic scale as in Equation (6), using the REGRESS procedure in IDL.

For the second method, we obtain the following relation:

$$\frac{M}{M_{\odot}} = 10^{7.16 \pm 0.04} \left(\frac{L_{P\alpha}}{10^{42} \text{ erg s}^{-1}} \right)^{0.49 \pm 0.06} \left(\frac{\text{FWHM}_{P\alpha}}{10^3 \text{ km s}^{-1}} \right)^2. \quad (9)$$

$$\frac{M}{M_{\odot}} = 10^{7.13 \pm 0.02} \left(\frac{L_{P\beta}}{10^{42} \text{ erg s}^{-1}} \right)^{0.48 \pm 0.03} \left(\frac{\text{FWHM}_{P\beta}}{10^3 \text{ km s}^{-1}} \right)^2. \quad (10)$$

In Figure 9, we compare the input M_{BH} versus M_{BH} from the Paschen estimators of the 2nd method. We find that the estimators in Equation (9) and (10) reproduce M_{BH} with rms scatters of about 0.20-0.24 dex, not much from the method 1.

In the third method, we treat all the coefficients in Equation (6) as free parameters. To derive the coefficients in the relation, we use a multiple variable linear regression fit with the REGRESS fitting procedure in IDL.

For the third method, we obtain the following relation:

$$\frac{M}{M_{\odot}} = 10^{7.31} \left(\frac{L_{P\alpha}}{10^{42} \text{ erg s}^{-1}} \right)^{0.48 \pm 0.03} \left(\frac{\text{FWHM}_{P\alpha}}{10^3 \text{ km s}^{-1}} \right)^{1.68 \pm 0.12} \quad (11)$$

$$\frac{M}{M_{\odot}} = 10^{7.40} \left(\frac{L_{P\beta}}{10^{42} \text{ erg s}^{-1}} \right)^{0.46 \pm 0.02} \left(\frac{\text{FWHM}_{P\beta}}{10^3 \text{ km s}^{-1}} \right)^{1.41 \pm 0.09} \quad (12)$$

Figure 10 shows the comparison of the input M_{BH} versus M_{BH} from the estimators in Equations (11) and (12). The rms scatter in the derived M_{BH} is reduced to 0.19, 0.21 dex while the exponents of the velocity term are found to be about 1.4-1.7 rather than the value of 2 expected in a virial relation. Compared to the 2nd method, the third method improves the fitting accuracy by a small amount in terms of reducing the rms scatter by 0.03 dex.

Also, note that the scatter in the M_{BH} estimator is intrinsic (e.g., the uncertainty in the input M_{BH} values) rather than dominated by the measurement errors in the FWHM and line luminosity measurements. The estimated $1\text{-}\sigma$ errors in FWHM and line luminosity measurements are 0.04 dex and 0.05 dex respectively, and such errors can produce a scatter in the M_{BH} estimators at the level of 0.09 dex only.

4. DISCUSSION

4.1. Consistency between three M_{BH} estimators

We derived the M_{BH} estimators in three different ways. Ideally, each estimator should give a M_{BH} value consistent with the others within the intrinsic rms scatter for a given set of realistic FWHM and line luminosity. To see if there is any noticeable deviation among the derived BH

mass values from the three different estimators, we compare M_{BH} values derived from the three estimators. For the input sets of FWHM and line luminosities, we convert the available $\text{H}\beta$ FWHM and $L(5100)$ of SDSS quasars from Shen et al. (2008) to the Paschen line quantities, which gives realistic sets of FWHM and line luminosity values in a large range of FWHM and luminosity parameter space occupied by quasars. To convert $\text{FWHM}_{\text{H}\beta}$ to $\text{FWHM}_{\text{P}\alpha}$ or $\text{FWHM}_{\text{P}\beta}$ and $L(5100)$ to $L_{\text{P}\alpha}$ and $L_{\text{P}\beta}$, we use the empirical relations presented in Section 3.1 of this paper. The derived Paschen line FWHM and luminosities are fed into the new M_{BH} estimators.

Figure 12 shows the comparison of M_{BH} derived from three different estimators. The left panel of the figure shows the comparison between M_{BH} values from the method 1 against those from the method 2. There is a small systematic offset of 0.1, 0.15 dex in the derived M_{BH} values at $M_{\text{BH}} \sim 10^{10.0} M_{\odot}$, $M_{\text{BH}} \sim 10^{7.0} M_{\odot}$ with the overall rms scatter of 0.06 dex. Considering that the rms scatter in these two estimators is about 0.2 dex, these two estimators produce M_{BH} values well within the rms scatter in their relation. The right panel of the Figure 12 compares M_{BH} from the method 2 versus the method 3. There is a significant systematic offset of 0.2 dex at the high mass end of $10^{10} M_{\odot}$ and the low mass end of $10^7 M_{\odot}$ – both are comparable the rms scatter of the M_{BH} estimators. The systematic offset results mainly from the difference in the exponent of FWHM in the M_{BH} estimators. The derived M_{BH} is proportional to FWHM^2 in the method 2, while M_{BH} from the method 3 is proportional to $\text{FWHM}^{1.5}$. Therefore, the method 2 is bound to produce M_{BH} values larger than the method 3 at large M_{BH} while the opposite trend appears at low M_{BH} .

It is difficult to determine which method gives the best estimate of M_{BH} . The method 3 gives the smallest scatter, but the FWHM exponent of 1.5 is less physical than the index of 2 in the method 2. The estimator from the method 3 may be proved to be the best choice, if a good explanation can be provided why the exponent of FWHM is 1.5, not 2. The M_{BH} estimator from the method 3 has a resemblance to the fundamental plane relation of early-type galaxies (Dressler et al. 1987; Djorgovski 1987) where it still remains controversial why the relation is slightly tilted off from the virial relation (e.g., see Jun & Im 2008), so a similar physical mechanism that produces the tilt in the fundamental plane might be in work for the M_{BH} estimator. For now, we prefer the method 2 the most simply because the formula can be justifiable easily on a physical basis.

4.2. Line Ratios

The line ratios of $\text{H}\beta$ through $\text{P}\alpha$ lines can give us clues on the physical conditions of the BLR region. The line ratios can also serve as a basis for determining the extinctions at different wavelengths in BLR of dusty AGN. Therefore, we present the line ratios of the Hydrogen lines of our sample.

Figure 11 shows the line ratios of $\text{H}\beta$, $\text{H}\alpha$, $\text{P}\beta$ to $\text{P}\alpha$ of our sample. Overplotted are theoretical line ratios based on the computation from the CLOUDY code (Ferland et al. 1998). Using the CLOUDY code, we calculate the expected line ratios by varying three parameters, the shape of the ionizing continuum ($\alpha = -1.0, -1.5$), the ionization parameter ($U = 10^{0.5}, 10^{-0.5}, 10^{-1.5}$) and the hydrogen density ($n = 10^9, 10^{10}, 10^{11} \text{ cm}^{-3}$). We find that the observed line ratios are reproduced most successfully with a set of parameters, $\alpha = -1.0$, $U = 10^{-1.5}$ and $n = 10^9 \text{ cm}^{-3}$. Some line ratios that are below the theoretical expectation can be explained naturally if there is a small amount of extinction with color excess of $E(B - V) < 0.4 \text{ mag}$. The mean line ratios are found to be $\frac{\text{H}\beta}{\text{P}\alpha} = 2.70$, $\frac{\text{H}\alpha}{\text{P}\alpha} = 9.00$, and $\frac{\text{P}\beta}{\text{P}\alpha} = 0.91$. These values can be used as a basis for determining extinctions in the BLR of dusty AGN. The perfect fit of the line ratios as a function of wavelengths is probably not possible with a simple model, considering that the broad emission lines at different wavelengths are not likely to originate from exactly the same BLR regions as we discussed in Section 3.1. Nevertheless, the observed line ratios are consistent with the expected ratios from a single set of ionization parameters.

5. CONCLUSION

We derived new M_{BH} estimators, using Hydrogen $\text{P}\alpha$ and $\text{P}\beta$ lines of Type-1 AGNs. The derived estimator allows the determination of M_{BH} at the accuracy of ~ 0.2 dex, and they will be useful for estimating M_{BH} of red, dusty AGNs. Our analysis of the Paschen lines with respect to $\text{H}\alpha$ and $\text{H}\beta$ lines shows that the luminosities and FWHMs of the broad components of the Paschen lines correlate well with those of the Balmer lines. The Hydrogen line ratios from $\text{H}\beta$ through $\text{P}\alpha$ are consistent with a Case B recombination with the parameters of $\alpha = -1.0$, $U = 10^{-1.5}$ and $n = 10^9 \text{ cm}^{-3}$. The mean line ratios are $\frac{\text{H}\beta}{\text{P}\alpha} = 2.70$, $\frac{\text{H}\alpha}{\text{P}\alpha} = 9.00$, and $\frac{\text{P}\beta}{\text{P}\alpha} = 0.91$ which can be used to estimate for the amount of dust extinction present in red AGNs in future. Future applications of these results on red, dusty AGNs will enable us to better understand the nature of red, dusty AGNs whose properties are still hidden behind a wall of dusty gas.

We thank the referee for useful comments which improved the manuscript. This work was supported by the grant No. 2009-063616 of the Creative Initiative Program, funded by the Korea government (MEST).

REFERENCES

- Bentz, M. C., Peterson, B. M., Netzer, H., Pogge, R. W., & Vestergaard, M. 2009, ApJ, 697, 160
 Bundy, K., et al. 2006, ApJ, 651, 120
 Comastri, A., Fiore, F., Vignali, C., Matt, G., Perola, G. C., & La Franca, F. 2001, MNRAS, 327, 781
 Dibai, E. A. 1977, Soviet Astron. Lett., 3, 1
 Djorgovski, S., & Davis, M. 1987, ApJ, 313, 59
 Dressler, A., Lynden-Bell, D., Burstein, D., Davies, R. L., Faber, S. M., Terlevich, R. J., & Wegner, G. 19 87, ApJ, 313, 42
 Ferland, G. J., Korista, K. T., Verner, D. A., Ferguson, J. W., Kingdon, J. B., & Verner, E. M. 1998, PASP, 110, 761
 Ferrarese, L., & Merritt, D. 2000, ApJ, 539, L9
 Gebhardt, K., et al. 2000, ApJ, 539, L13
 Glikman, E., Helfand, D. J., White, R. L., Becker, R. H., Gregg, M. D., & Lacy, M. 2007, ApJ, 667, 673

- Glikman, E., Helfand, D. J., & White, R. L. 2006, *ApJ*, 640, 579
Greene, J. E., & Ho, L. C. 2005, *ApJ*, 630, 122
Greene, J. E., & Ho, L. C. 2007, *ApJ*, 670, 92
Hopkins, P. F., & Hernquist, L. 2006, *ApJS*, 166, 1
Im, M., Griffiths, R. E., & Ratnatunga, K. U. 1997, *ApJ*, 475, 457
Imanishi, M., Miolino, R., & Nakagawa, T. 2010, *ApJ*, 709, 801
Jun, H., & Im, M. 2008, *ApJ*, 678, L97
Juneau, S., et al. 2005, *ApJ*, 619, L135
Kaspi, S., Smith, P. S., Netzer, H., Maoz, D., Jannuzi, B. T., & Giveon, U. 2000, *ApJ*, 533, 631
Kim, M., Ho, L. C., & Im, M. 2006, *ApJ*, 642, 702
Landt, H., Bentz, M. C., Ward, M. J., Elvis, M., Peterson, B. M., Korista, K. T., & Karovska, M. 2008, *ApJS*, 174, 282
McGill, K. L., Woo, J.-H., Treu, T., & Malkan, M. A. 2008, *ApJ*, 673, 703
Meyers, K. A., & Peterson, B. M. 1985, *PASP*, 97, 734
Onken, C. A., Ferrarese, L., Merritt, D., Peterson, B. M., Pogge, R. W., Vestergaard, M., & Wandel, A. 2004, *ApJ*, 615, 645
Peterson, B. M., et al. 2004, *ApJ*, 613, 682
Polletta, M., Weedman, D., Hönig, S., Lonsdale, C. J., Smith, H. E., & Houck, J. 2008, *ApJ*, 675, 960
Rayner, J. T., Toomey, D. W., Onaka, P. M., Denault, A. J., Stahlberger, W. E., Vacca, W. D., Cushing, M. C., & Wang, S. 2003, *PASP*, 115, 362
Schawinski, K., et al. 2006, *Nature*, 442, 888
Schneider, D. P., et al. 2003, *AJ*, 126, 2579
Skrutskie, M. F., et al. 2006, *AJ*, 131, 1163
Tozzi, P., et al. 2006, *A&A*, 451, 457
Tremaine, S., et al. 2002, *ApJ*, 574, 740
Urrutia, T., Becker, R. H., White, R. L., Glikman, E., Lacy, M., Hodge, J., & Gregg, M. D. 2009, *ApJ*, 698, 1095
Véron, P., Gonçalves, A. C., & Véron-Cetty, M.-P. 2002, *A&A*, 384, 826
Vestergaard, M., & Peterson, B. M. 2006, *ApJ*, 641, 689
Woo, J.-H., et al. 2010, *arXiv:1004.0252*

TABLE 1
PASCHEN PARAMETERS AND BH MASSES

| AGNs Name | Redshift z | BHmass $\log(M/M_{\odot})$ | P β | | | | P α | | | |
|-------------------------------------|---------------|-------------------------------|-------------------------------|--|---|--|-------------------------------|--|---|--|
| | | | FWHM [km s ⁻¹] | Δ FWHM [km s ⁻¹] | Flux [erg s ⁻¹ cm ⁻²] | Δ flux [erg s ⁻¹ cm ⁻²] | FWHM [km s ⁻¹] | Δ FWHM [km s ⁻¹] | Flux [erg s ⁻¹ cm ⁻²] | Δ flux [erg s ⁻¹ cm ⁻²] |
| 3C273 ^a | 0.158 | 8.94 ^c | 2608 | – | 6.95E-13 | – | 2635 | – | 8.33E-13 | – |
| Mrk876 ^a | 0.129 | 8.44 ^c | 5433 | – | 7.81E-14 | – | 4965 | – | 1.31E-13 | – |
| PG0844+349 ^a | 0.064 | 7.96 ^c | 2144 | – | 1.06E-13 | – | 1967 | – | 1.21E-13 | – |
| Mrk110 ^a | 0.035 | 7.40 ^c | 1689 | – | 1.50E-13 | – | 1604 | – | 1.99E-13 | – |
| Mrk509 ^a | 0.034 | 8.15 ^c | 2755 | – | 5.20E-13 | – | 2747 | – | 6.60E-13 | – |
| Ark120 ^a | 0.033 | 8.17 ^c | 4610 | – | 5.89E-13 | – | 4584 | – | 6.96E-13 | – |
| Mrk817 ^a | 0.031 | 7.69 ^c | 4988 | – | 1.39E-13 | – | 4202 | – | 1.39E-13 | – |
| Mrk335 ^a | 0.026 | 7.15 ^c | 1633 | – | 1.67E-13 | – | 1431 | – | 1.40E-13 | – |
| Mrk590 ^a | 0.026 | 7.67 ^c | 3565 | – | 1.46E-14 | – | 4259 | – | 2.82E-14 | – |
| NGC5548 ^a | 0.017 | 7.82 ^c | 5891 | – | 1.77E-13 | – | 4102 | – | 1.64E-13 | – |
| NGC4151 ^a | 0.003 | 7.12 ^c | 4204 | – | 1.21E-12 | – | – | – | – | – |
| H1821+643 ^a | 0.297 | 9.44 ^d | 4717 | – | 1.92E-13 | – | – | – | – | – |
| PDS456 ^a | 0.184 | 8.70 ^d | 1828 | – | 3.79E-13 | – | 1785 | – | 4.70E-13 | – |
| Mrk290 ^a | 0.030 | 8.09 ^d | 3818 | – | 1.55E-13 | – | 3180 | – | 1.64E-13 | – |
| H2106–099 ^a | 0.027 | 7.72 ^d | 2155 | – | 1.70E-13 | – | 1550 | – | 2.35E-13 | – |
| Mrk79 ^a | 0.022 | 7.94 ^d | 3163 | – | 1.86E-13 | – | 3051 | – | 2.58E-13 | – |
| NGC4593 ^a | 0.009 | 7.83 ^d | 3407 | – | 2.87E-13 | – | – | – | – | – |
| NGC3227 ^a | 0.004 | 7.42 ^d | 2680 | – | 3.48E-13 | – | – | – | – | – |
| HE 1228+013 ^a | 0.117 | 7.87 ^d | 1731 | – | 6.62E-14 | – | 1725 | – | 7.46E-14 | – |
| H1934–063 ^a | 0.011 | 6.80 ^d | 1241 | – | 1.37E-13 | – | 1213 | – | 1.77E-13 | – |
| IRAS1750+508 ^a | 0.300 | 8.33 ^d | 1758 | – | 4.50E-14 | – | – | – | – | – |
| SDSSJ000943.1–090839.2 ^b | 0.210 | 8.44 ^e | 4817 | 818 | 8.41E-15 | 1.84E-15 | 3841 | 724 | 8.31E-15 | 2.10E-15 |
| SDSSJ005812.8+160201.3 ^b | 0.211 | 8.29 ^e | 3158 | 409 | 1.73E-14 | 1.96E-15 | 2775 | 357 | 2.23E-14 | 2.37E-15 |
| SDSSJ010226.3–003904.6 ^b | 0.295 | 7.67 ^e | 1565 | 184 | 2.42E-14 | 1.87E-15 | 1234 | 142 | 2.86E-14 | 2.04E-15 |
| SDSSJ011110.0–101631.8 ^b | 0.179 | 8.20 ^e | 3695 | 496 | 1.48E-14 | 1.77E-15 | 2617 | 380 | 1.41E-14 | 1.99E-15 |
| SDSSJ015530.0–085704.0 ^b | 0.165 | 8.85 ^e | 7355 | 1032 | 1.53E-14 | 2.38E-15 | 5074 | 737 | 1.36E-14 | 2.24E-15 |
| SDSSJ015910.0+010514.5 ^b | 0.217 | 7.98 ^e | 2657 | 404 | 1.01E-14 | 1.48E-15 | 2574 | 455 | 1.02E-14 | 1.89E-15 |
| SDSSJ015950.2+002340.8 ^b | 0.163 | 8.09 ^e | 2657 | 391 | 2.65E-14 | 2.53E-15 | 2716 | 627 | 3.78E-14 | 3.99E-15 |
| SDSSJ021707.8–084743.4 ^b | 0.292 | 7.84 ^e | 1970 | 552 | 3.49E-15 | 1.14E-15 | – | – | – | – |
| SDSSJ024250.8–075914.2 ^b | 0.378 | 8.00 ^e | 1329 | 194 | 9.28E-15 | 1.15E-15 | – | – | – | – |
| SDSSJ031209.2–081013.8 ^b | 0.265 | 8.29 ^e | 3540 | 620 | 1.12E-14 | 2.01E-15 | – | – | – | – |
| SDSSJ032213.8+005513.4 ^b | 0.185 | 8.03 ^e | 2014 | 234 | 2.58E-14 | 1.89E-15 | 1894 | 220 | 3.40E-14 | 2.47E-15 |
| SDSSJ150610.5+021649.9 ^b | 0.135 | 8.11 ^e | – | – | – | – | 2632 | 330 | 2.26E-14 | 2.54E-15 |
| SDSSJ172711.8+632241.8 ^b | 0.218 | 8.61 ^e | – | – | – | – | 5087 | 1192 | 1.13E-14 | 2.86E-15 |
| SDSSJ211843.2–063618.0 ^b | 0.328 | 8.42 ^e | 2485 | 430 | 6.58E-15 | 1.29E-15 | – | – | – | – |
| SDSSJ234932.7–003645.8 ^b | 0.279 | 8.19 ^e | 2578 | 360 | 1.02E-14 | 1.47E-15 | – | – | – | – |
| SDSSJ235156.1–010913.3 ^b | 0.174 | 8.89 ^e | 6137 | 705 | 4.42E-14 | 3.53E-15 | 4946 | 553 | 5.14E-14 | 3.65E-15 |

^a FWHM and Flux of these objects come from L08.

^b FWHM and Flux of these objects measured from spectra presented in G06.

^c The M_{BH} values are determined from reverberation mapping techniques (Vestergaard & Peterson 2006).

^d The M_{BH} values are based on H β widths and luminosities in L08.

^e The M_{BH} values are based on H β widths and L(5100) derived from our fit to SDSS spectra.

TABLE 2
 COEFFICIENTS OF THE EMPIRICAL CORRELATION BETWEEN BALMER AND PASCHEN LINES

| Num | Y | X | FWHM | | | Line luminosity | | |
|-----|------------|------------|-------------------|-------------------|-----------|-------------------|-------------------|-----------|
| | | | A | B | rms (dex) | C | D | rms (dex) |
| 1 | H α | P α | 0.074 \pm 0.038 | 0.934 \pm 0.084 | 0.045 | 0.916 \pm 0.014 | 0.961 \pm 0.025 | 0.141 |
| 2 | H β | P α | 0.105 \pm 0.037 | 1.017 \pm 0.080 | 0.057 | 0.444 \pm 0.013 | 0.910 \pm 0.018 | 0.188 |
| 3 | H α | P β | 0.076 \pm 0.038 | 0.821 \pm 0.075 | 0.051 | 0.985 \pm 0.012 | 1.008 \pm 0.015 | 0.117 |
| 4 | H β | P β | 0.113 \pm 0.033 | 0.895 \pm 0.068 | 0.058 | 0.517 \pm 0.011 | 0.943 \pm 0.013 | 0.162 |

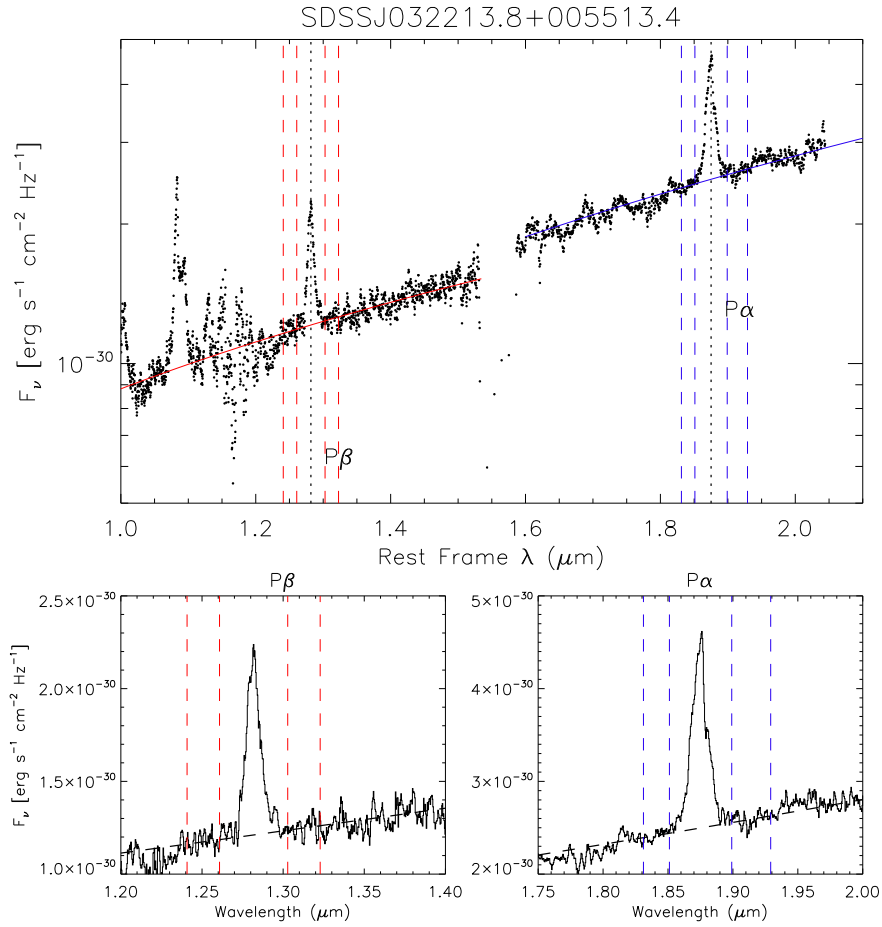


FIG. 1.— An example of the continuum fitting of the G06 NIR spectra. On the top panel, we show the NIR spectrum of SDSSJ032213.8+005513.4, where the blue solid line indicates the continuum fit to the $P\alpha$ wavelength region and the red solid line shows the continuum fit to the $P\beta$ wavelength area. The wavelength ranges that were used for determining the continuum are indicated with the vertical dashed lines. In the bottom panels, we show the expanded views around $P\beta$ and $P\alpha$ lines together with the determined continuum.

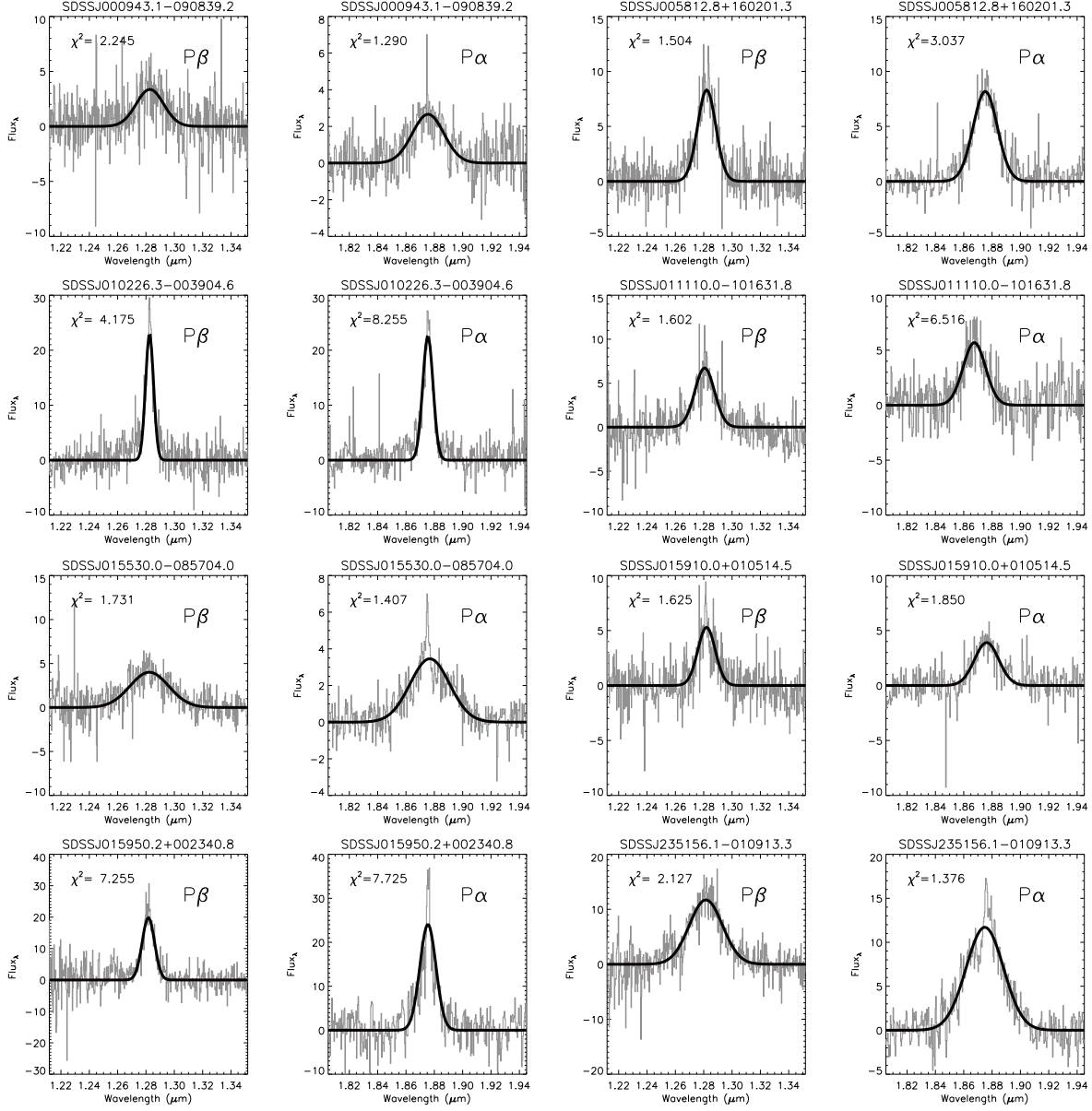


FIG. 2.— Results of the fitting of Paschen lines with a Gaussian function to the G06 sample. AGNs with both $P\alpha$ and $P\beta$ measurements are shown here. The ordinate is in units of $10^{-17} \text{ erg s}^{-1} \text{ cm}^{-2} \mu\text{m}^{-1}$. The continuum is already subtracted. The black solid line indicates the best-fit and the grey solid line indicate observed spectrum.

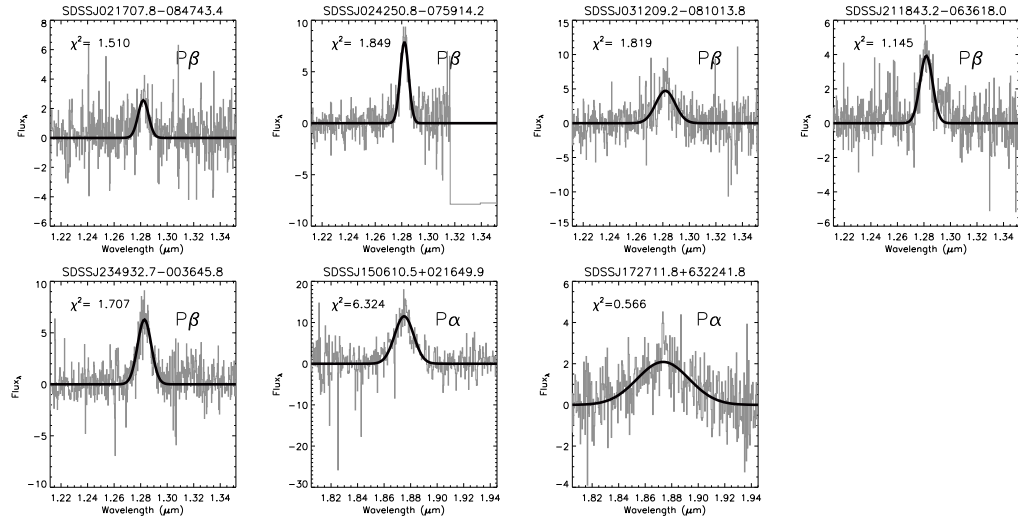


FIG. 3.— Gaussian fits of the Paschen lines of the G06 sample. AGNs with only P α or P β measurements are shown here. The meaning of the lines is identical to Figure 3.

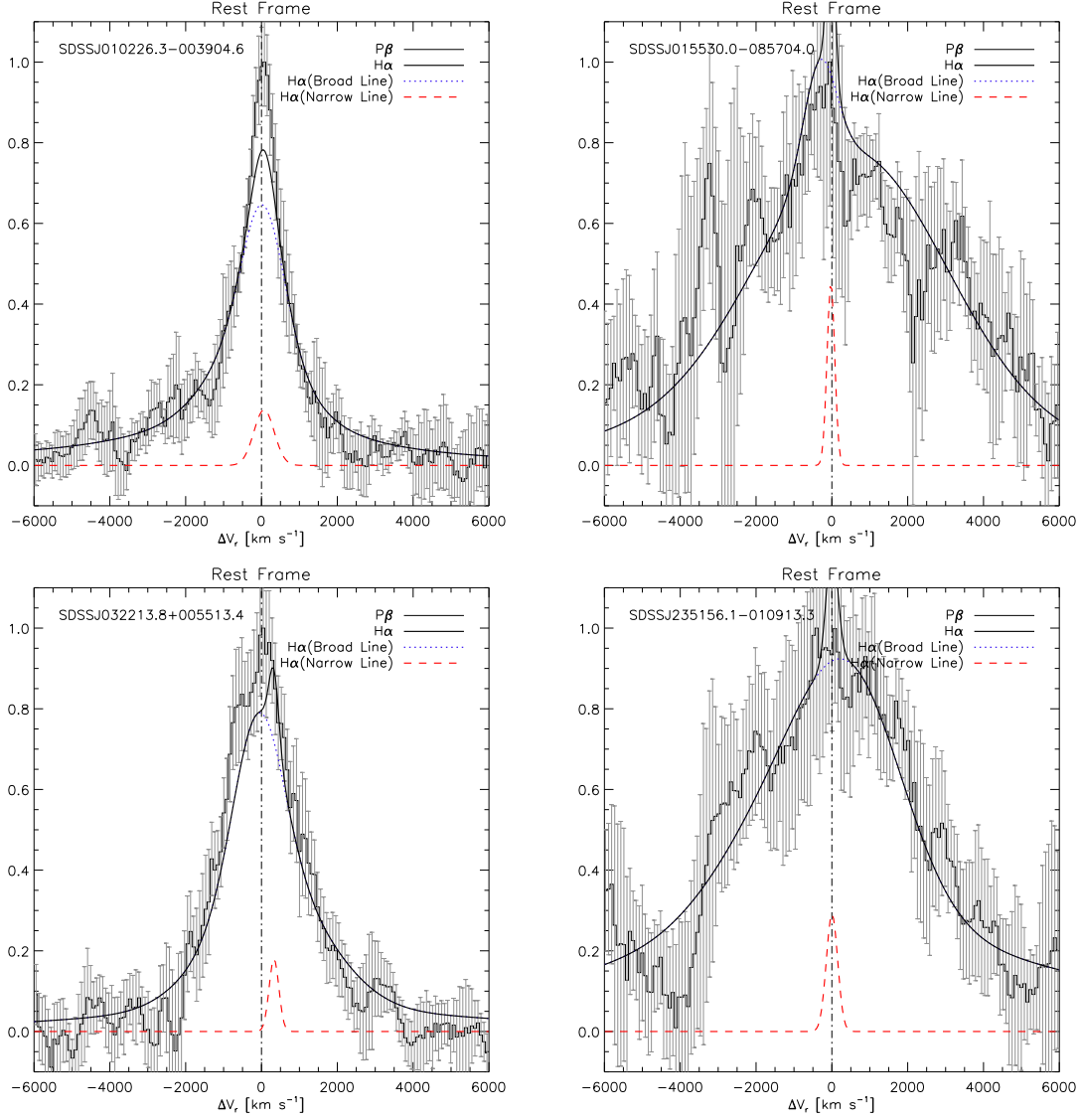


FIG. 4.— The comparison of the $P\beta$ line profiles against the $H\alpha$ line profiles. Only objects with $P\beta$ line $S/N > 25$ are shown here (histogram with errors). The $H\alpha$ lines are indicated with thick solid lines, and the thin dotted lines and the thick dashed lines represent the broad and the narrow components of the $H\alpha$ lines. The $P\beta$ profiles are normalized to have the maximum value of 1 while the $H\alpha$ are normalized to have the same total flux as the normalized $P\beta$ profiles. The figure shows that the $P\beta$ line profile shapes are consistent with the $H\alpha$ profile shapes.

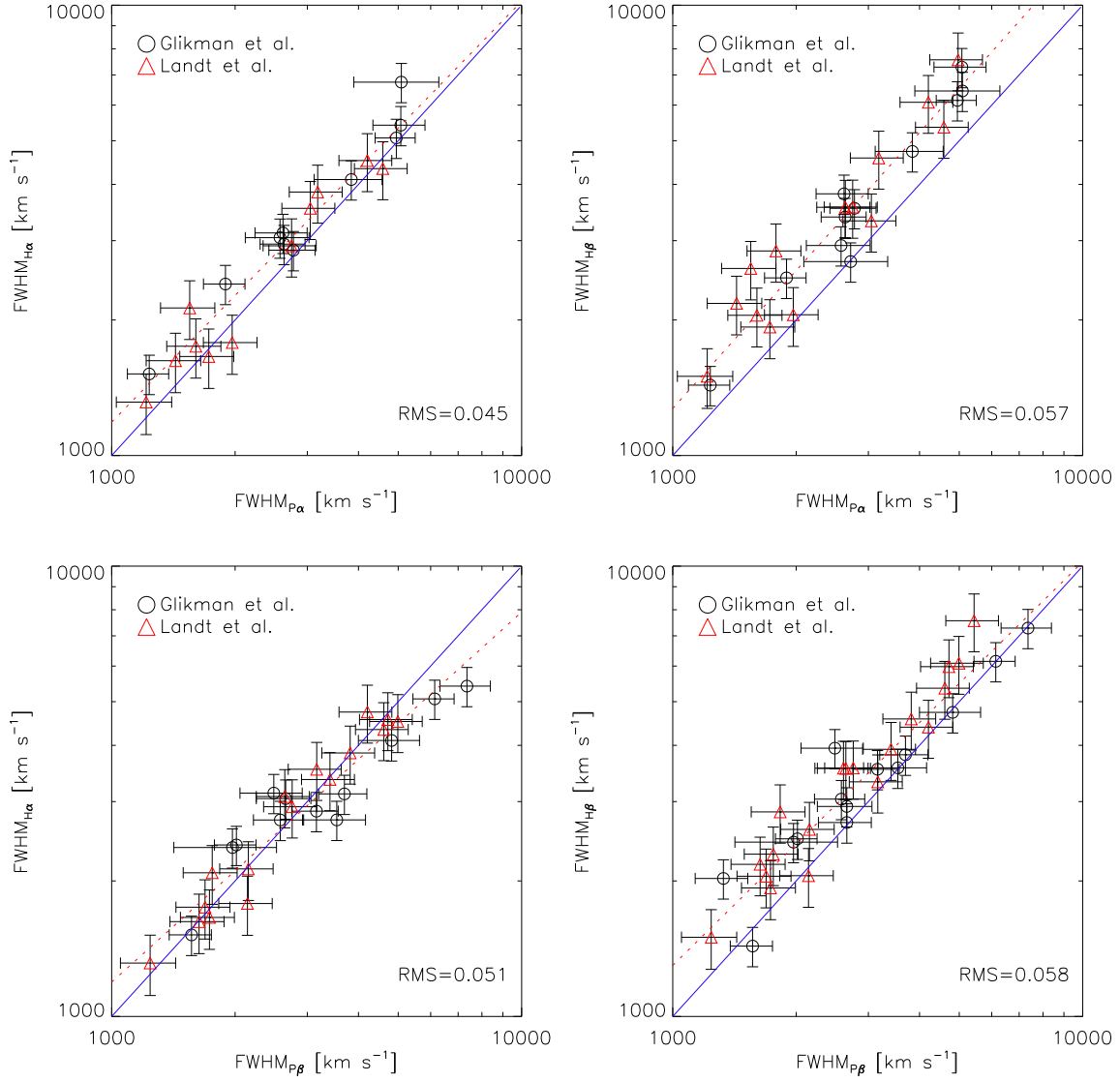


FIG. 5.— The comparison of the FWHM widths of the Paschen lines versus the Balmer lines. The top panels compare the $\text{P}\alpha$ FWHMs versus the Balmer line FWHMs, while the bottom panels show the comparison of the $\text{P}\beta$ FWHMs versus the Balmer line FWHMs. The open circles are for AGNs from G06, while the red triangles are for the L08 sample. The solid line indicates a line where the Balmer and the Paschen quantities are identical. The dotted line indicates the best-fit line between the two quantities as described in the text.

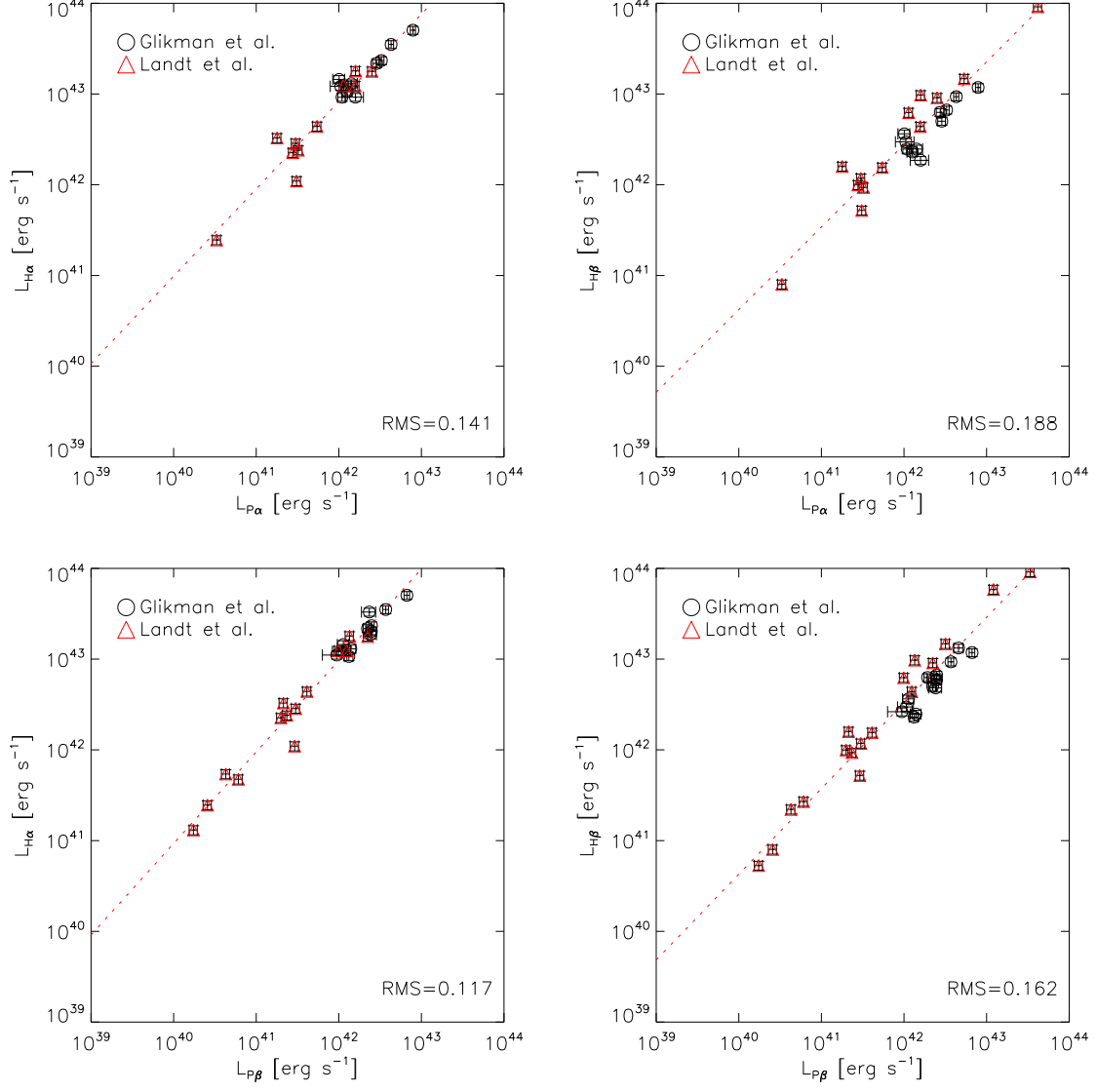


FIG. 6.— The comparison of the Paschen line luminosities against those of the Balmer lines. The top two panels compare the $\text{P}\alpha$ fluxes against the Balmer lines fluxes, while the bottom two panels compare the $\text{P}\beta$ fluxes against the Balmer line fluxes. The symbols are same as those in Figure 5. The meaning of dotted line is identical to that in Figure 5.

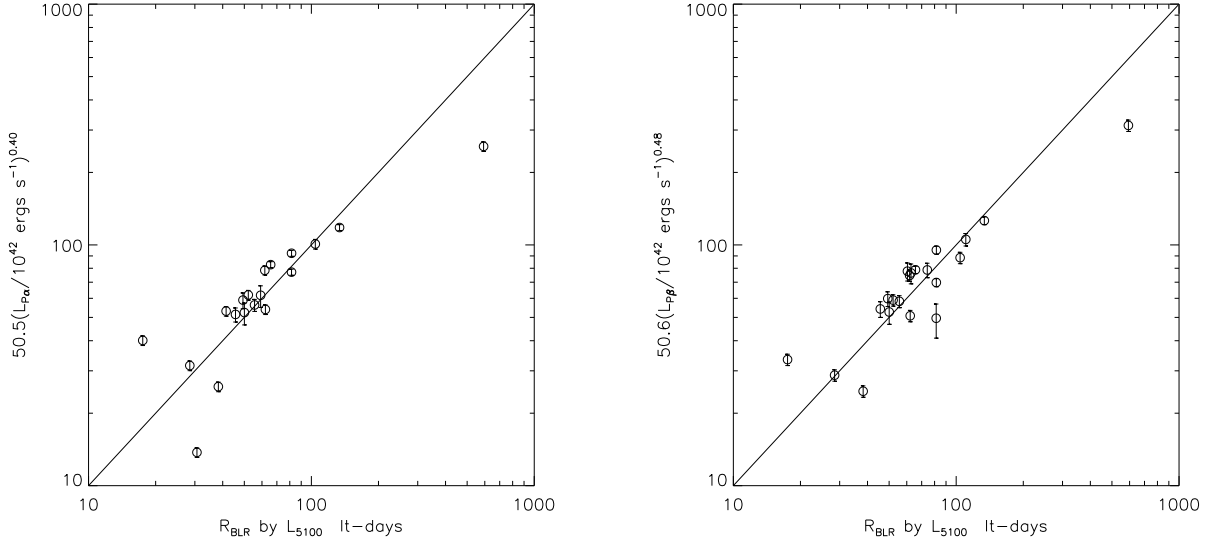


FIG. 7.— The correlation between the $P\alpha$ (left) and the $P\beta$ (right) luminosities and the BRL sizes. The BLR sizes are derived from the 5100\AA luminosities. The good correlation (albeit over 40 lt-days to 110 lt-days) suggests that the Paschen line luminosities can be used to estimate the BLR size. The solid lines indicate the best-fit relation of the correlation.

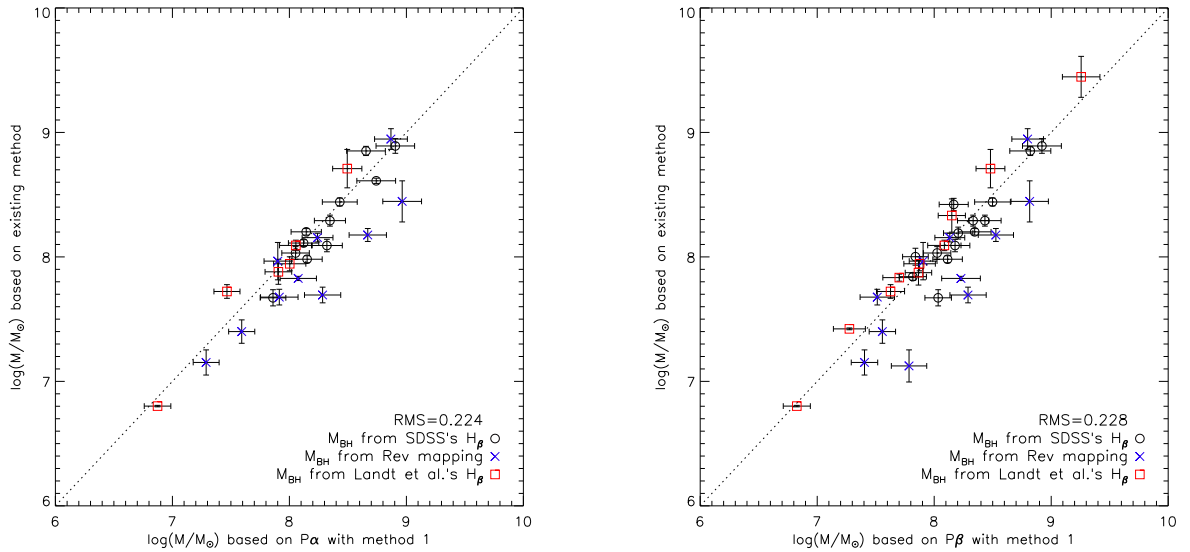


FIG. 8.— Comparison of the Paschen-line based M_{BH} versus M_{BH} derived from the reverberation mapping or optical spectra using the 1st method described in the text. Black circles indicate the G06 sample. Blue crosses show the L08 sample with M_{BH} derived from the reverberation mapping (Vestergaard & Peterson 2006). Red squares are for the L08 sample with M_{BH} estimated from single epoch optical spectra. The solid line indicates an one to one function with M_{BH} based on existing method and it upon properties of Paschen line.

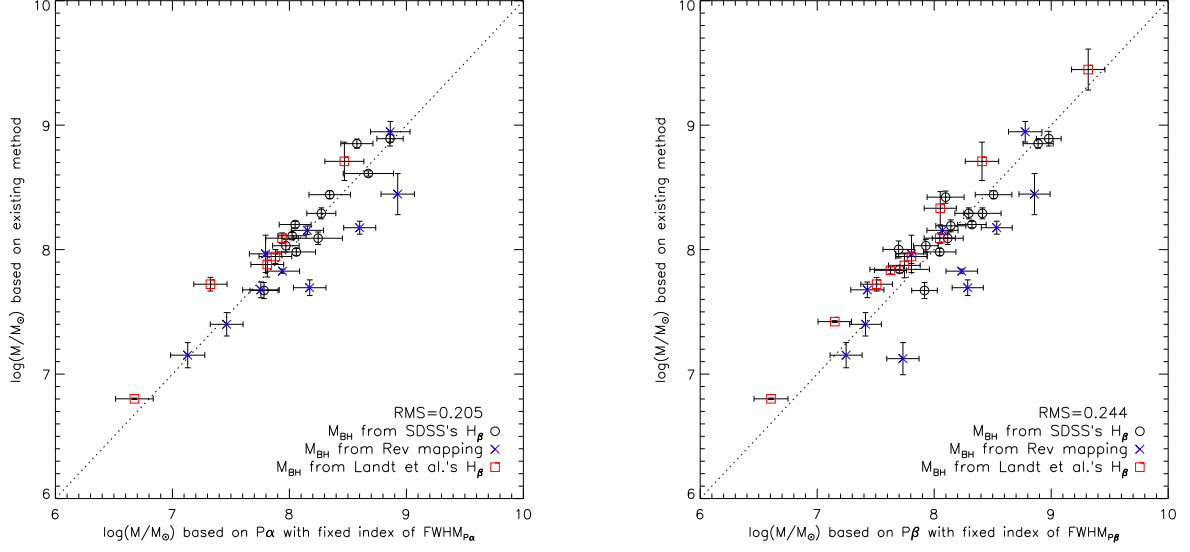


FIG. 9.— Similar to Figure 8, but with the Paschen-based M_{BH} where M_{BH} are derived with an estimator for which the power-law index of FWHM is fixed to 2. The meaning of the symbols and line are identical to Figure 8.

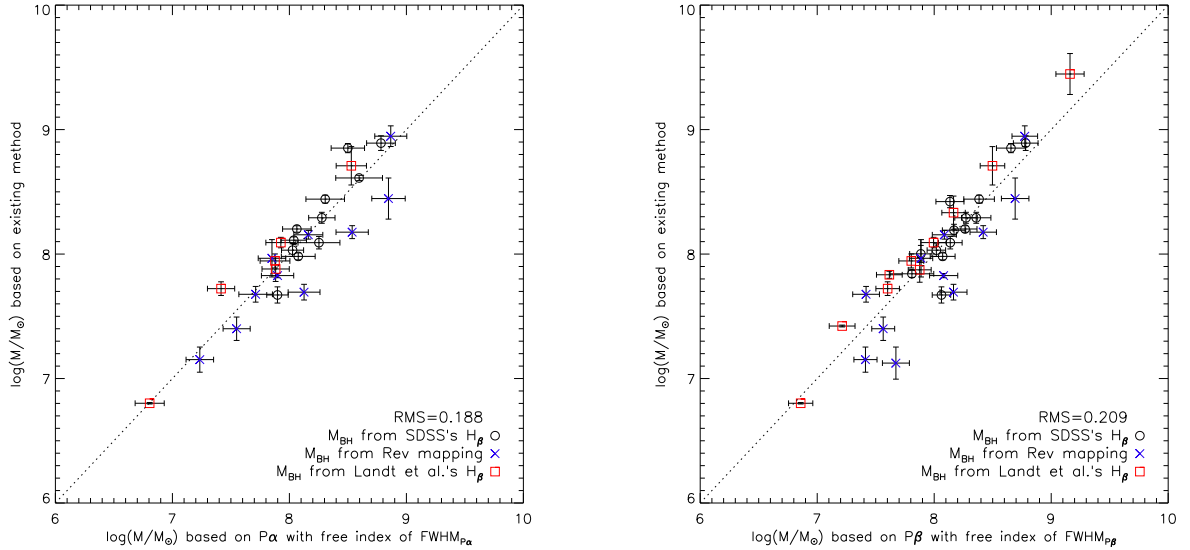


FIG. 10.— Similar to Figure 8, but with the Paschen-based M_{BH} where M_{BH} are derived with an estimator for which the power-law index of FWHM is set free during the fit. The meaning of the symbols and line are identical to Figure 8.

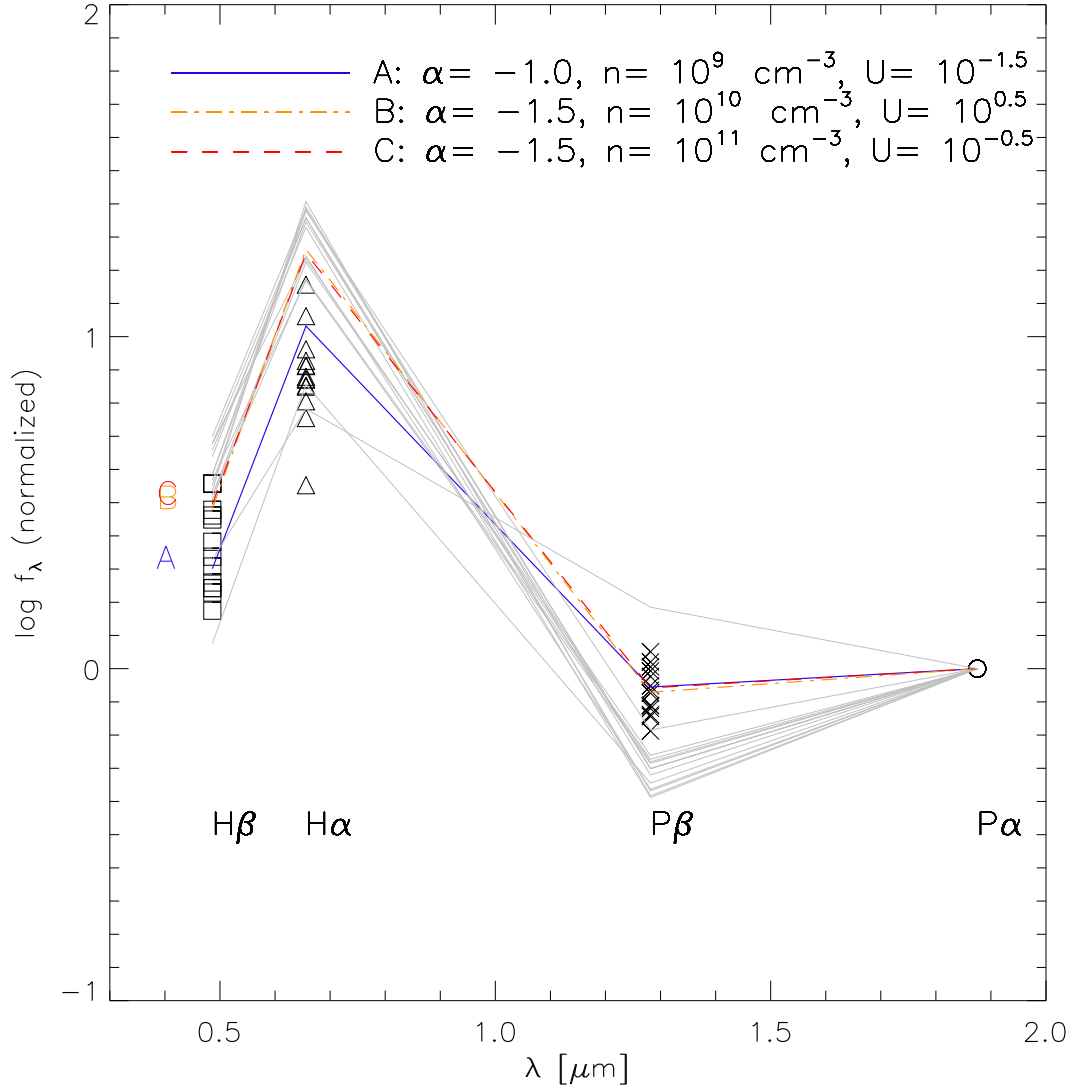


FIG. 11.— Line ratio of type-1 AGNs compared with theoretical models from CLOUDY code. Fluxes are normalized to that of P α . These models show that typical type 1 AGN condition is $\alpha = -1.0$, $n = 10^9 \text{ cm}^{-3}$ and $U = 10^{-1.5}$. The grey lines are theoretical models from various condition, within $\alpha = -1.5 \sim -1.0$, $n = 10^9 \sim 10^{11} \text{ cm}^{-3}$ and $U = 10^{-1.5} \sim 10^{0.5}$.

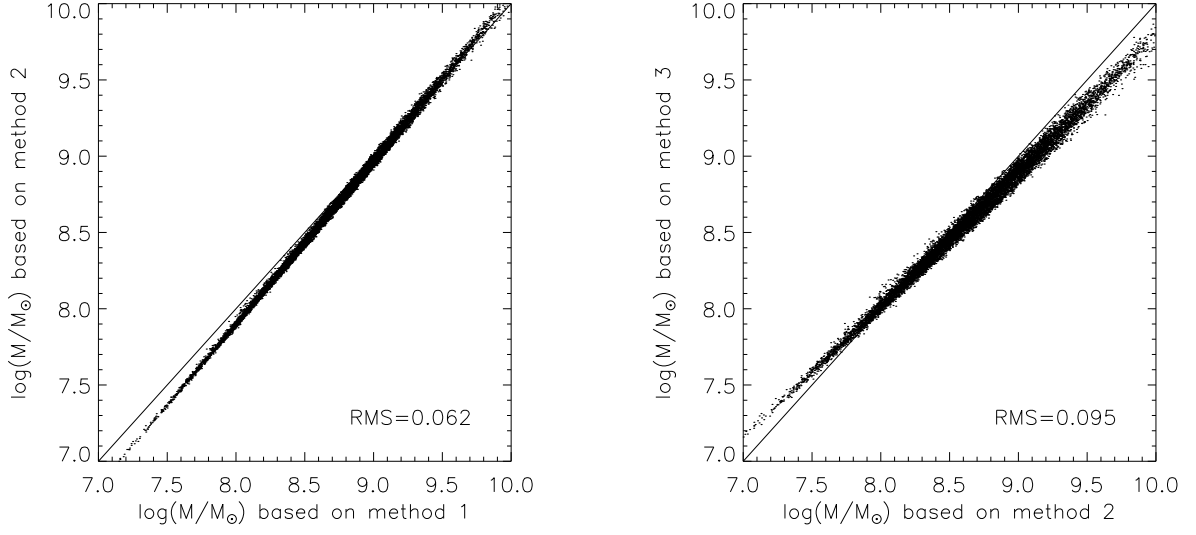


FIG. 12.— The left panel compares M_{BH} from the method 1 and the method 2. In the right panel, we compare M_{BH} from the method 2 versus the method 3. The M_{BH} values agree well with each other in this case. The data points come from SDSS DR5 quasars in Shen et al. (2008) where the Paschen FWHM and luminosities are estimated from the corresponding $H\beta$ quantities. The solid line indicates the case where the BH masses derived from different methods are identical.